



# Nonlinear Evolution of Short-wavelength Torsional Alfvén Waves

S. V. Shestov<sup>1,4</sup>, V. M. Nakariakov<sup>2,3</sup>, A. S. Ulyanov<sup>4</sup>, A. A. Reva<sup>4</sup>, and S. V. Kuzin<sup>4</sup>

<sup>1</sup> Solar-Terrestrial Centre of Excellence—SIDC, Royal Observatory of Belgium, Avenue Circulaire 3, B-1180 Brussels, Belgium; [s.shestov@oma.be](mailto:s.shestov@oma.be)

<sup>2</sup> Centre for Fusion, Space and Astrophysics, Department of Physics, University of Warwick, Coventry CV4 7AL, UK

<sup>3</sup> St. Petersburg Branch, Special Astrophysical Observatory, Russian Academy of Sciences, 196140, St. Petersburg, Russia

<sup>4</sup> Lebedev Physical Institute, Leninskii prospekt, 53, 119991, Moscow, Russia

Received 2017 March 20; revised 2017 April 5; accepted 2017 April 6; published 2017 May 5

## Abstract

We analyze nonlinear evolution of torsional Alfvén waves in a straight magnetic flux tube filled in with a low- $\beta$  plasma, and surrounded with a plasma of lower density. Such magnetic tubes model, in particular, a segment of a coronal loop or a polar plume. The wavelength is taken comparable to the tube radius. We perform a numerical simulation of the wave propagation using ideal magnetohydrodynamics. We find that a torsional wave nonlinearly induces three kinds of compressive flows: the parallel flow at the Alfvén speed, which constitutes a bulk plasma motion along the magnetic field, the tube wave, and also transverse flows in the radial direction, associated with sausage fast magnetoacoustic modes. In addition, the nonlinear torsional wave steepens and its propagation speed increases. The latter effect leads to the progressive distortion of the torsional wave front, i.e., nonlinear phase mixing. Because of the intrinsic non-uniformity of the torsional wave amplitude across the tube radius, the nonlinear effects are more pronounced in regions with higher wave amplitudes. They are always absent at the axes of the flux tube. In the case of a linear radial profile of the wave amplitude, the nonlinear effects are localized in an annulus region near the tube boundary. Thus, the parallel compressive flows driven by torsional Alfvén waves in the solar and stellar coronae, are essentially non-uniform in the perpendicular direction. The presence of additional sinks for the wave energy reduces the efficiency of the nonlinear parallel cascade in torsional Alfvén waves.

**Key words:** magnetohydrodynamics (MHD) – Sun: corona – Sun: oscillations – waves

**Supporting material:** animation

## 1. Introduction

The existence of plane Alfvén waves was theoretically predicted by Alfvén (1942), and since then the ubiquitous presence of Alfvén waves was found in magnetospheric, space, cosmic, and laboratory plasmas (e.g., Cheng et al. 1985; Uberoi 1995; Chaston et al. 2000). In solar physics, Alfvén waves are mainly considered to be candidates for coronal heating due to their ability to freely propagate from lower layers of the solar atmosphere to the corona (e.g., Ruderman 1999; Srivastava et al. 2017). For example, Copil et al. (2008) suggested that propagating Alfvén waves could locally heat coronal plasma threads. In addition, Fletcher & Hudson (2008) proposed that a flare-generated large-scale torsional wave could accelerate electrons to high energies. Alfvén waves may also contribute to the acceleration of the solar and stellar winds (e.g., Charbonneau & MacGregor 1995; Cranmer 2009; Matsumoto & Suzuki 2012), and collimate astrophysical jets (Bisnovaty-Kogan 2007).

In the presence of field-aligned plasma non-uniformities, typical for the corona, Alfvén waves appear in the form of torsional waves (e.g., Van Doorselaere et al. 2008). Torsional Alfvén waves are azimuthal (rotational) perturbations of the plasma velocity accompanied by azimuthal components of the magnetic field. Linear torsional waves propagate along the magnetic field at the local Alfvén speed.

The key element of the nonlinear evolution of linearly and elliptically polarized Alfvén waves is the ponderomotive force that is associated with the variation of the absolute value of the magnetic field in the wave (e.g., Hollweg 1971; Tikhonchuk et al. 1995). This variation results in the gradient of the magnetic pressure that induces plasma flows and hence changes

the density of the plasma. The induced compressive perturbations have double the frequency of the mother Alfvén wave. The induced variations of the absolute value of the magnetic field and plasma density change the local values of the Alfvén speed, and cause the Alfvén wave self-interaction resulting in steepening of the wave front (e.g., Ofman & Davila 1995; Zheng et al. 2016).

Nonlinear dynamics of Alfvén waves are actively studied analytically and numerically, with the main emphasis put on the study of plane waves. It has been shown that weakly nonlinear plane Alfvén waves are governed by the Cohen–Kulsrud evolutionary equation, which is a modification of the well-known Burgers equation, accounting for the cubic nonlinearity intrinsic to Alfvén waves (e.g., Cohen & Kulsrud 1974). In addition, when the wave front is non-plane or oblique, Alfvén waves induce oblique compressive perturbations (e.g., Malara et al. 1996; Nakariakov et al. 1997). The ponderomotive acceleration effects have been intensively studied in the context of acceleration of the solar and stellar winds (e.g., Ofman & Davila 1998; Nakariakov et al. 2000; Suzuki 2011), and also of the first ionization potential effect (e.g., Laming 2015).

Nonlinear evolution of plane Alfvén waves is strongly affected by transverse structuring of the plasma in the Alfvén speed and/or field-aligned plasma flows. The transverse structuring of the medium leads to the wave front distortion, the wave becomes progressively non-planar, and the effect of phase mixing comes into play. It causes enhanced dissipation of Alfvén waves (e.g., Heyvaerts & Priest 1983; Hood et al. 2002) and induces compressive perturbations that produce fast and slow magnetoacoustic waves (e.g., Nakariakov et al. 1997, 1998; Botha et al. 2000; Tsiklauri & Nakariakov 2002; Tsiklauri et al. 2003).

However, in a plane wave, the perpendicular scale, i.e., the length of the wave front, should be much larger than the parallel wavelength, which is rarely fulfilled. For example, in the solar corona, the generation of a plane Alfvén wave with a 10 minute period and the Alfvén speed of  $1 \text{ Mm s}^{-1}$  the wave driver at the base of the corona should be much larger than 600 Mm (i.e., much larger than the radius of the Sun). Because the solar corona is structured into magnetic flux tubes, represented, for example, by coronal loops, plumes, and various filaments, coronal Alfvén waves are likely to appear in the form of torsional, rather than plane perturbations. Torsional waves have received attention in the context of heating of the plasma in coronal loops. In particular, Poedts & Boynton (1996) and Ruderman et al. (1997) considered dissipation of finite-amplitude waves driven periodically at one footpoint of a closed magnetic structure. On the other hand, Antolin & Shibata (2010) established several constraints on the parametric range of Alfvén waves as a coronal heating mechanism.

The understanding of the appearance of coronal Alfvén waves in the torsional form stimulated intensive studies of nonlinear evolution of torsional waves. Kudoh & Shibata (1999) and Vasheghani Farahani et al. (2011) numerically and analytically, respectively, demonstrated that propagating torsional Alfvén waves, similarly to plane waves, induce compressive perturbations due to the ponderomotive force associated with nonlinear effects. Vasheghani Farahani et al. (2012) found that weakly nonlinear self-interaction of torsional Alfvén waves results in the Cohen–Kulsrud steepening of the wave profile, while the coefficients are different from the case of a plane wave. The self-interaction occurs due to the nonlinear excitation of compressive waves and their back-reaction on the mother torsional waves. Fedun et al. (2011) showed by means of numerical simulations that chromospheric magnetic flux tubes can act as a frequency filter for torsional waves. Mikhalyaev & Bembitov (2014) analytically studied the resonant generation of compressive waves by nonlinear coupling of two torsional waves propagating in the opposite directions. Murawski et al. (2015) and Wójcik et al. (2017) highlighted the effect of the expanding magnetic tube on the evolution of torsional Alfvén waves and emphasized the importance of the stratification. Williams et al. (2016) modeled the propagation of torsional waves in the presence of slow compressive shocks.

However, the efficiency of nonlinear interaction of torsional and compressive waves is not understood in detail so far. In particular, the role of the transverse profile of the torsional wave needs to be revealed. The main motivation for this study is the intrinsic non-uniformity of the wave fronts of torsional waves. Indeed, as the finite-amplitude effects increase the wave propagation speed (e.g., Cohen & Kulsrud 1974), and as the torsional wave has a zero amplitude at the axis of the guiding magnetic flux tube and increases to the tube boundary, the propagation speed is always non-uniform across the field. It creates the conditions for phase mixing even if the Alfvén speed inside the flux tube is uniform, because the torsional waves have different nonlinear increase in the propagation speed at different distance from the tube axis. This nonlinear phase mixing leads to the generation of compressive perturbations. The induced compressive perturbations may lead to the torsional wave self-interaction. Also, in contrast with the incompressible Alfvén waves, the induced compressive

perturbations can be detected with imaging telescopes and are subject to enhanced damping by various dissipative mechanisms.

The aim of this paper is to study by means of 3D magnetohydrodynamic (MHD) modeling the effects of nonlinear excitation of compressive perturbations by a torsional wave of finite amplitude. We consider the parallel wavelength to be not much larger than the radius of the magnetic flux tube, and thus account for the nonlinear phase mixing. This approach is a finite-wavelength generalization of the analytical theory developed by Vasheghani Farahani et al. (2011) in the thin flux tube approximation that corresponds to the long-wavelength limit. We neglect the effect of the stratification of the atmosphere, as the typical radii of coronal field-aligned plasma non-uniformities and hence the considered wavelengths are about 1–10 Mm, while the typical scale heights of the stratification exceed 50 Mm. Thus, we consider the evolution of torsional waves in a flux tube that is uniform along its axis. The paper is organized as follows. In Section 2, we describe our numerical setup, in Section 3, we discuss the results obtained, and we finally give conclusions in Section 4. Appendix A illustrates the nonlinear excitation of compressive perturbations by a long-wavelength torsional waves in the thin flux tube approximation, and Appendix B illustrates the generation of compressive waves due to the phase mixing effect.

## 2. Numerical Setup and Initial Conditions

### 2.1. MHD Equations and Normalization

The simulations were performed using the numerical code MPI-AMRVAC (Porth et al. 2014). The code applies the Eulerian approach to the solution of the resistive MHD equations,

$$\frac{\partial \rho}{\partial t} + \nabla \cdot (\rho \mathbf{v}) = 0, \quad (1)$$

$$\frac{\partial (\rho \mathbf{v})}{\partial t} + \nabla \cdot (\mathbf{v} \rho \mathbf{v} - \mathbf{B} \mathbf{B}) + \nabla p_{\text{tot}} = 0, \quad (2)$$

$$\frac{\partial \mathbf{B}}{\partial t} + \nabla \cdot (\mathbf{v} \mathbf{B} - \mathbf{B} \mathbf{v}) = -\nabla \times (\eta \mathbf{J}), \quad (3)$$

$$\frac{\partial e}{\partial t} + \nabla \cdot (\mathbf{v} e - \mathbf{B} \mathbf{B} \cdot \mathbf{v} + \mathbf{v} p_{\text{tot}}) = \nabla \cdot (\mathbf{B} \times \eta \mathbf{J}), \quad (4)$$

where  $e$ ,  $\rho$ ,  $\mathbf{v}$ , and  $\mathbf{B}$  are the total energy density, mass density, velocity, and magnetic field,  $p = (\gamma - 1)(e - \rho v^2/2 - B^2/2)$  is the thermal pressure,  $p_{\text{tot}} = p + B^2/2$  is the total pressure,  $\mathbf{J} = \nabla \times \mathbf{B}$  is the electric current density;  $\eta$  is the electrical resistivity, and  $\gamma$  is the ratio of specific heats. Because, in this study, we are not interested in dissipative processes, we take  $\gamma = 5/3$ , and  $\eta = 0$ .

The physical quantities were normalized with the use of the following constants: the lengths are normalized to  $L_N = 1 \text{ Mm}$ , magnetic fields to  $B_N = 20 \text{ G}$ , and densities to  $\rho_N = 1.67 \times 10^{-15} \text{ g cm}^{-3}$ . The mass density normalization corresponds to the electron concentration  $n_N = 10^9 \text{ cm}^{-3}$ . The normalizing speed was calculated in units of  $v_N = B_N / \sqrt{4\pi\rho_N} = 1,380 \text{ km s}^{-1}$ , that is, the Alfvén speed corresponding to the values of  $B_N$  and  $\rho_N$ , the normalizing time was set to  $t_N = L_N / v_N = 0.7246 \text{ s}$ , the normalization of the radial derivative of the azimuthal velocity was set to

$\Omega_N = v_N/L_N = 1.38 \text{ s}^{-1}$ . The values used for the normalization are typical for the solar corona; their use justifies our intention to analyze nonlinear effects in the coronal plasma. Further in the text, we imply normalized units if it is not stated otherwise.

### 2.2. Numerical Setup

We used a cylindrical frame of reference, and considered a straight magnetic tube directed along the  $z$ -axis of the computational box. The equilibrium magnetic field is parallel to the tube axis. The equilibrium concentration of electrons,  $n_e(r)$  was set using the generalized symmetric Epstein function (Cooper et al. 2003), and the equilibrium parallel magnetic field  $B_z(r)$  was set to equalize the equilibrium total pressure everywhere in the computational box,

$$\begin{cases} n_e(r) = n_\infty + \frac{(n_0 - n_\infty)}{\cosh^2[(r/R_0)^\alpha]} \\ B_z(r) = B_0 \left\{ 1 + \frac{4T(n_0 - n_\infty)}{B_0^2} \right. \\ \quad \left. \times \left( 1 - \frac{1}{\cosh^2[(r/R_0)^\alpha]} \right) \right\}^{1/2}, \end{cases} \quad (5)$$

where  $R_0 = 1$  is the tube radius,  $n_\infty = 0.2$ ,  $n_0 = 1$ ,  $B_0 = 1$ , and the temperature  $T$  is constant throughout the whole volume. In physical units, these values correspond to  $R_0 = 1 \text{ Mm}$ ,  $n_\infty = 2 \times 10^8 \text{ cm}^{-3}$ ,  $n_0 = 10^9 \text{ cm}^{-3}$ , and  $B_0 = 20 \text{ G}$ , i.e., typical for the corona. The parameter  $\alpha$  controls the tube boundary steepness. We used  $\alpha = 36$ , which results in a rather sharp boundary. The radial profiles of the electron density  $n_e(r)$  and magnetic field  $B_z(r)$  are depicted in Figure 1.

All the equilibrium values are constant along the  $z$ -axis, since we consider neither gravity nor transition region in this study.

The torsional Alfvén wave is driven at the bottom wall  $z = z_{\min} = 0$  of the equilibrium magnetic flux tube by the following perturbations,

$$\begin{aligned} B_\varphi(r) &= J_M r \frac{\sin(\omega t)}{\cosh^2[(r/R_0)^\alpha]}, \\ v_\varphi(r) &= \Omega_M r \frac{\sin(\omega t)}{\cosh^2[(r/R_0)^\alpha]}, \end{aligned} \quad (6)$$

where  $J_M$  is the amplitude of the radial derivative of the azimuthal component of the magnetic field,  $\Omega_M = -J_M/\sqrt{4\pi\rho(r)}$  is the amplitude of the radial derivative of the azimuthal component of the velocity, and the factor  $\cosh^2[(r/R_0)^\alpha]$  is introduced to avoid the excitation of the torsional wave outside the tube. The frequency  $\omega$  is set to  $\omega = \omega_A = 2\pi/\lambda C_A$ , where  $\lambda$  is a wavelength. The top boundary is set to keep zero gradients of the variables (the `cont` flag in MPI-AMRVAC). In this study, we consider the waves before they reach the top boundary, and hence the specific choice of the top boundary condition is not important.

### 2.3. Parameters of Numerical Experiments

We analyzed dynamics of the torsional Alfvén wave, controlling the following parameters: the plasma temperature

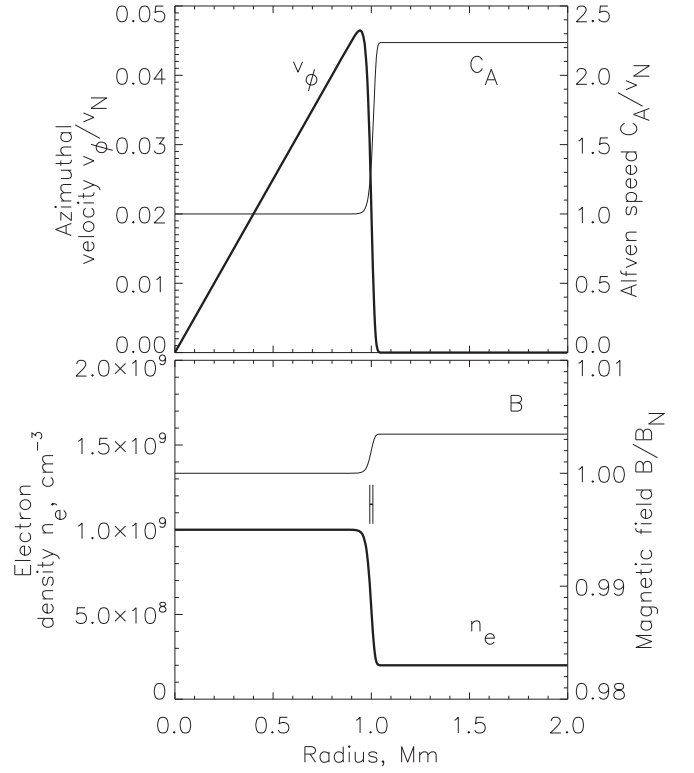


**Figure 1.** Top: radial profiles of the normalized initial azimuthal velocity  $v_\varphi(r)$  and equilibrium Alfvén speed  $C_A(r)$  in the simulated magnetic flux tube. Bottom: radial profiles of the equilibrium electron density  $n_e(r)$  and normalized equilibrium magnetic field  $B_z(r)$ . The line segment at the point  $(1.0, 10^9)$  in the bottom panel indicates the scale of a single pixel used during the simulation.

**Table 1**  
Parameters of the Simulations

Title	$T$ (MK)	$\lambda$ (Mm)	$\Omega_M$	Plasma $\beta$
setup1	0.2	5.0	0.05	0.0035
setup2	0.2	10.0	0.05	0.0035
setup3	1.0	2.0	0.05	0.0173
setup4	1.0	5.0	0.05	0.0173
setup5	1.0	10.0	0.05	0.0173
setup6	1.0	10.0	0.075	0.0173
setup7	1.0	10.0	0.10	0.0173
setup8	1.0	10.0	0.15	0.0173
setup9	1.0	10.0	0.20	0.0173
setup10	5.0	10.0	0.05	0.087

**Note.** The plasma temperature  $T$ , the wavelength  $\lambda$ , the initial amplitude of the radial derivative of the azimuthal velocity perturbation  $\Omega_M$  (normalized), and the plasma parameter  $\beta$ .

$T$  (and hence, for the fixed value of  $B_0$ , on the plasma parameter  $\beta$  that is the ratio of the gas and magnetic pressures), amplitude of the derivative of the azimuthal velocity perturbation,  $\Omega_M$ , and wavelength  $\lambda$ . The specific values of these parameters in various numerical runs are shown in Table 1.

In all of these setups, the relative variation of the magnetic field is small, and the plasma- $\beta$  is less than unity everywhere.

The simulations were performed in a cylindrical frame of reference, in either a 3D  $(r, \varphi, z)$  or 2D  $(r, z)$  computational boxes. We used a 3D computational box for the investigation of the general picture of the wave propagation, and

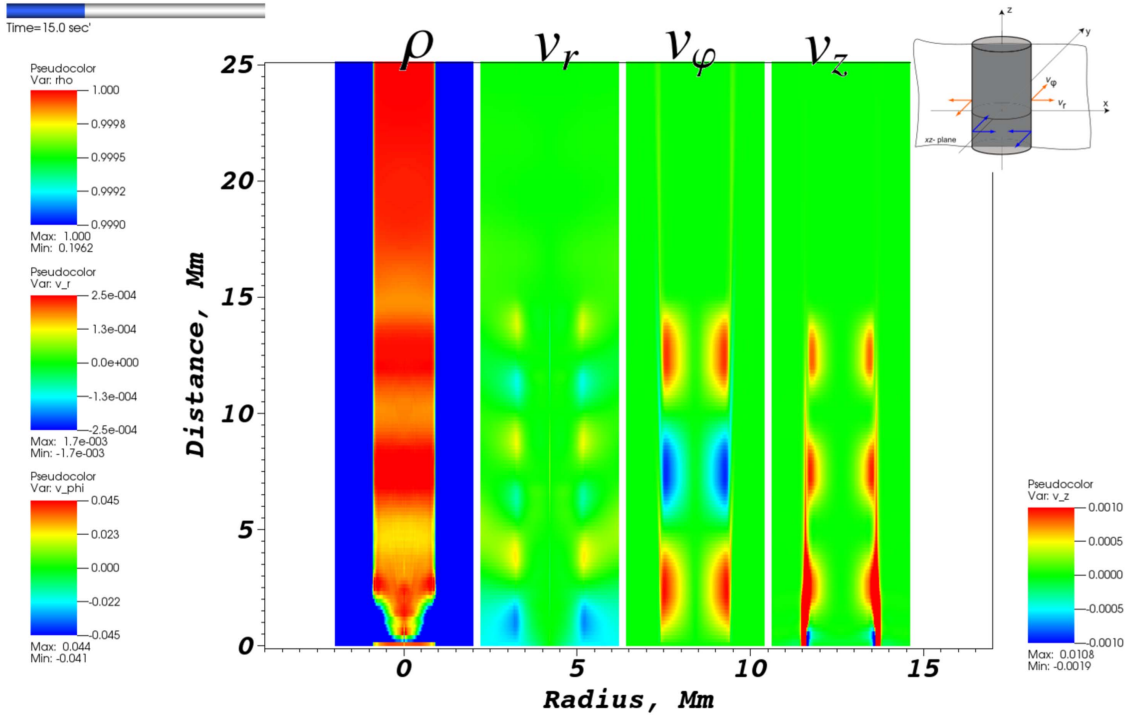


**Figure 2.** Torsional Alfvén wave propagating along the magnetic flux tube. The panels show the spatial structure of the plasma density  $\rho$  and velocities  $v_r$ ,  $v_\phi$ ,  $v_z$  (from left to right) in the  $xz$  cross-section through the axis of the flux tube, shown in the inset. The torsional Alfvén wave is excited at  $z = 0$ , and propagates in the positive  $z$ -direction (upward). The snapshot corresponds to setup 5, i.e.,  $T = 1$  MK,  $\lambda = 10$  Mm,  $\Omega_M = 0.05$ ; the time instant is  $t = 15t_N = 10.9$  s.

(An animation of this figure is available.)

high-resolution 2D computational boxes were used for the analysis of wave-steepening, radial profiles and generation of sausage waves.

In the 3D case, the box size was  $128 \times 64 \times 256$  grid points, which corresponds to the physical volume  $[0, 2]$  Mm in  $r$ ,  $[0, 2\pi]$  in  $\phi$ , and  $[0, 40]$  Mm in  $z$ . The numerical grid (pixel) size corresponds to  $0.0156$  Mm in  $r$  (see Figure 1) and  $0.156$  Mm in  $z$ , i.e., much less than the characteristic scales of the non-uniformity and wavelength. In order to test the undesirable effect of the grid resolution, we carried out a test run with double the spatial resolution. We found that, in both of the cases, the evolution of the torsional wave shows similar behavior, in general, but the setup with the lower spatial resolution demonstrated faster decay and a smoother wave profile at the tube boundary.

In 2D simulations, we used different grids. For the investigation of wave steepening, we used the numerical grid  $384 \times 2048$ , with  $r \in [0, 3]$  Mm and  $z \in [0, 80]$  Mm, respectively. For the investigation of the radial profiles of the perturbations, we used the numerical grid  $1024 \times 256$ , with  $r \in [0, 2]$  Mm and  $z \in [0, 20]$  Mm, respectively, and for the investigation of sausage magnetoacoustic wave generation, we used the grid  $384 \times 8192$ , with  $r \in [0, 3]$  Mm and  $z \in [0, 320]$  Mm. In all of the cases, the spatial resolution in the “important” dimension was much higher than in the 3D setup.

In MPI-AMRVAC, we choose either HLLC (for 3D simulations), or the `ssprk54` (for 2D simulations) discretization method, with the `vanleer` slope limiter. The constraint  $\nabla B = 0$  is controlled by the `powell` approach. Since we already analyzed the effect of numerical resolution on the results, we use no mesh refinement and set the parameter `mxnest` to 1.

### 3. Results and Discussion

#### 3.1. General Picture of Torsional Wave Propagation

In general, results of the simulation agree with the theory highlighted in Appendix A. A torsional wave appears as an alternate perturbation of the azimuthal plasma velocity accompanied by a perturbation of the azimuthal component of the magnetic field,  $B_\phi$ . The wave dynamics preserves the axial symmetry. Snapshots demonstrating perturbations of various physical quantities in the wave are shown in Figure 2. The wave is seen to propagate along the flux tube, in the positive  $z$ -direction, at the speed of about the Alfvén speed  $C_A$  in the body of the flux tube. At the time of the snapshots  $t_1 = 15t_N = 10.9$  s, the wave has propagated the distance  $l_1 = C_A t_1 \approx 15$  Mm  $= 1.5\lambda$  from the point of the excitation,  $z = 0$ .

The local Alfvén speed (see Figure 1) increases near the tube boundary, in a thin layer where the equilibrium plasma density decreases. This leads to the outrunning of the torsional wave near the tube boundaries, producing a distortion of the wave fronts. It is a clear signature of phase mixing caused by the transverse non-uniformity of the Alfvén speed. We refer to the effect as linear phase mixing and will further consider it in Section 3.7.

The detected torsional wave induces flows with two other velocity components, the radial velocity  $v_r$  and parallel velocity  $v_z$ , and also the density perturbations that propagate at the Alfvén speed and have double the frequency of the driver and the perturbations of the azimuthal velocity  $v_\phi$  and magnetic field  $B_\phi$ . The amplitudes of induced  $v_r$  and  $v_z$  amounts to square of the amplitude  $v_\phi$  of the initial wave.

In addition, in the bottom part of the computational domain (Figure 2), one can see the development of the tube wave



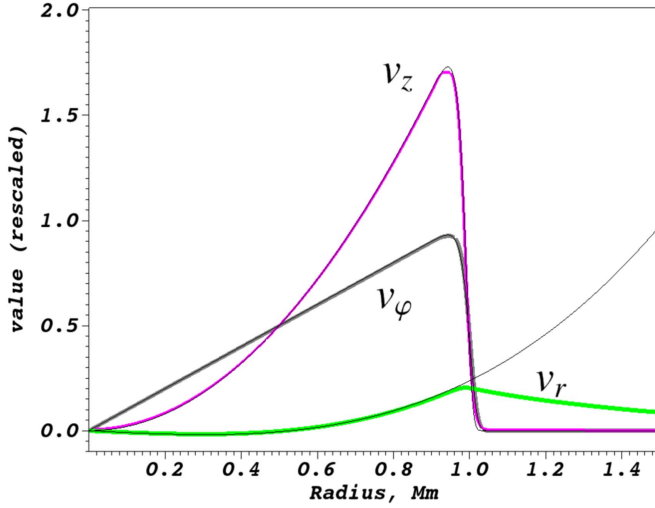


**Figure 3.** Radial profiles of  $v_r$ ,  $v_\phi$ , and  $v_z$  velocities in the wave maximum. Thick curves are results of numerical simulation: the black line shows the azimuthal velocity  $v_\phi$ , the magenta curve shows the parallel velocity  $v_z$ , and the green curve shows the radial velocity  $v_r$ . The profiles are rescaled for the purpose of visualization:  $v_\phi$  is divided by  $\Omega_M = 0.05$ , and  $v_z$  and  $v_r$  are divided by  $6.25 \times 10^{-4}$ . The thin curves indicate the best-fitting analytical dependencies.

propagating at the tube speed  $C_T \approx 0.15 \text{ Mm s}^{-1}$ . At the time of the snapshot, the wave has propagated the distance  $l_2 = C_T t_1 \approx 1.6 \text{ Mm}$  from the excitation point, which is consistent with Equation (26). The tube wave is excited when the plasma temperature is finite, and hence the tube speed  $C_T$  is greater than zero.

The appearance of the parallel compressive perturbations characterized by  $\rho$  and  $v_z$  may be attributed to the effect of the nonlinear ponderomotive force associated with the gradients of the perturbed Alfvén speed in the parallel direction, and that is in agreement with the theory developed in Vashghani Farahani et al. (2011), see also Equation (25). The excitation of the radial flows, which are compressive too, may be attributed to the nonlinear ponderomotive force associated with the gradients of the perturbed Alfvén speed in the perpendicular direction (Nakariakov et al. 1997), see also Appendix B, and to the effect of nonlinear phase mixing, connected with the radial non-uniformity of the torsional wave amplitude.

### 3.2. Radial Profiles of Induced Compressive Perturbations

The radial structure of the induced parallel flows at the speed  $v_z$ , obtained in the simulation (see Figure 3), is seen to be different from that described by expressions (8) and (27) obtained in the thin flux tube approximation. It clearly shows a parabolic shape,  $\propto r^2$ . This difference could be attributed to the finite-wavelength effects. A similar radial dependence is seen in the radial structure of the perturbed parallel magnetic field  $B_z$  (not shown here).

The simulated radial profile of  $v_z$  was found to be well fitted with an almost parabolic dependency,

$$v_z(r, z, t) = \frac{\Omega_M^2 r^2 (1 - \cos[2\omega(t - z/C_A)])}{4C_A \cosh^4[(r/R_0)^{36}]}, \quad (7)$$

determined empirically, by a guess. The radial dependence in the denominator is artificially used to reproduce the disappearance of the perturbation at the flux tube boundary. This parabolic dependence is different from the solution for  $u_p$ ,

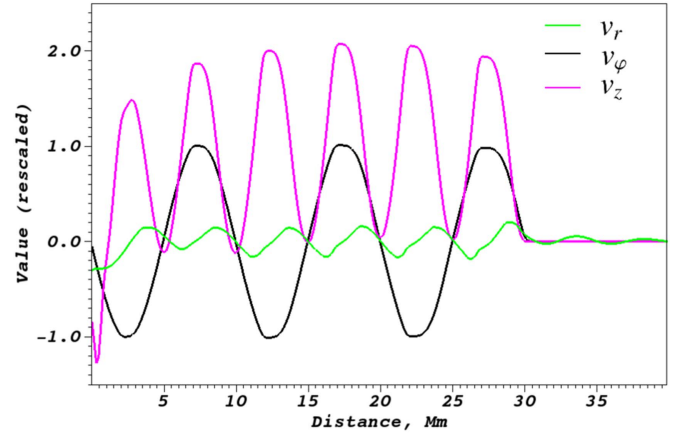


**Figure 4.** Spatial profiles of  $v_r$ ,  $v_\phi$ ,  $v_z$  velocities measured along the  $z$ -axis at  $r_1 = 0.75 \text{ Mm}$  at the time instant  $t = 30 t_N$ . The black curve shows the azimuthal velocity  $v_\phi$ , the magenta curve the parallel velocity  $v_z$ , and the green curve the radial velocity  $v_r$ . The profiles are rescaled for the purpose of visualization:  $v_\phi$  is divided by  $\Omega_M r_1 = 3.75 \times 10^{-2}$ , and  $v_r$  and  $v_z$  are divided by  $3.52 \times 10^{-4}$ .

given by Equation (27), which is independent of the radial coordinate  $r$ . We need to emphasize that the dependence given by Equation (7) is fully empirical, and is not based on any theoretical result. It is shown here for its possible usefulness for forward modeling of the observational manifestation of this effect, when it would be convenient to have a single functional expression for the radial structure of the induced parallel flows. The perturbations of the density  $\rho$  and pressure  $p$  do not show dependence on the radial coordinate, and have a constant amplitude across the flux tube.

The radial profiles of  $v_r$  and  $B_r$  are different from the other variables. They have half the wavelength of the mother torsional wave (given by the perturbations of  $v_\phi$  and  $B_\phi$ ), and are shifted by  $+\pi/4$  relative to the mother torsional wave. The radial structure of  $v_r$  can be expressed using the odd terms of the Taylor expansion (see Figure 3), beginning with the linear one that is prescribed by the boundary condition at the loop axis (see also the discussion in Zhugzhda 1996). In the performed numerical run, we found that the radial dependence of the radial velocity inside the flux tube could be best-fitted by the expression  $v_r(r) = 0.33r(r^2 - 0.28)$ . We note that the radial velocity has relatively large values outside the tube's boundary, whereas the azimuthal and parallel velocities do not penetrate into the external medium.

### 3.3. Parallel Spatial Structure of Induced Compressive Perturbations

Parallel spatial profiles of the velocities  $v_r$ ,  $v_\phi$ ,  $v_z$  measured along the  $z$ -axis at  $r_1 = 0.75 \text{ Mm}$  are shown in Figure 4. The profiles are rescaled for the purpose of visualization:  $v_\phi$  is divided by  $\Omega_M r_1 = 3.75 \times 10^{-2}$ , and  $v_r$  and  $v_z$  are divided by  $\Omega_M^2 r_1^2 / 4C_A = 3.52 \times 10^{-4}$ . This rescaling corresponds to the omitting of amplitudes and radial dependencies of the variables in Equations (6) and (7) (and with the caveat in Equations (26) and (27)). These profiles are consistent with the theory described in Appendix A: the wavelength of the induced parallel flows is half of the wavelength of the torsional wave, the induced parallel flows have a positive average value, and the amplitude corresponds to one given by Equation (25), i.e.,

the amplitude of induced parallel velocities is proportional to the squared amplitude of the azimuthal perturbation.

The positive average value of the parallel velocity means a field-aligned bulk plasma flow (e.g., see Ofman & Davila 1998), which can be referred to as the “Alfvénic wind.” The wind is produced by the ponderomotive force. However, the wind is canceled on the arrival of the slow, tube wave  $u_T$ . A similar effect has been studied in detail in the case of plane Alfvén waves by McLaughlin et al. (2011).

In addition, we see small amplitude perturbations of  $v_r$ . The amplitude of this perturbation is approximately five times smaller than the amplitude of parallel motions, and the speed of propagation in the  $z$ -direction is higher than the speed of the torsional wave. These perturbations correspond to the third kind of the induced compressive perturbations, the fast magnetoacoustic sausage wave (e.g., Edwin & Roberts 1983; Nakariakov et al. 2012; Yu et al. 2016). In the low- $\beta$  plasma considered here, this mode is characterized by compressive, mainly radial flows, and propagates at the speed that lies between the Alfvén speed inside and outside the tube. Positive and negative half-periods of these perturbations are symmetric. Hence, in contrast with the induced parallel flows, they do not constitute any bulk flow of the plasma.

### 3.4. Efficiency of the Generation of Compressive Perturbations

To study whether the efficiency of the nonlinear generation of compressive perturbations depends on various parameters of the plasma, such as the temperature  $T$ , wavelength  $\lambda$  and the tube’s radius, i.e., to check the validity of the approximation given by Equation (27), we perform a parametric study summarized in Table 1.

We analyzed amplitudes of the parallel velocity perturbations,  $v_z$ , in the leading cycle of the induced wave, at the distance of 10–15 Mm from the origin in Figure 2. According to Equation (27), the behavior of the induced ponderomotive wave depends neither on the temperature  $T$ , nor on the wavelength  $\lambda$ . For the amplitude of the ponderomotive wave, numerical setups with different plasma temperatures  $T$  and wavelength  $\lambda$  were found to show good agreement with Equation (27) near the boundary of the flux tube. In addition, we saw the tube wave propagating at the tube speed, which is consistent with Equation (26), again, near the boundary.

### 3.5. Nonlinear Wave Steepening

The ponderomotive excitation of compressive flows by an Alfvén wave, leads to the modification of the local Alfvén speed, which, in turn, affects the Alfvén wave itself. This chain of events is considered to be nonlinear self-interaction of the Alfvén wave, which leads to the wave steepening (e.g., Cohen & Kulsrud 1974). In the long-wavelength limit, steepening of a torsional wave due to nonlinear self-interaction has been considered by Vasheghani Farahani et al. (2012). In that study, it was found that the torsional wave steepening occurs at the rate that is lower than in the case of plane Alfvén waves. The difference between the evolution of the torsional and plane waves disappears in the case of the cold ( $\beta = 0$ ) plasma. In our work, we consider this effect on torsional waves of finite wavelength. For comparison, we modeled nonlinear evolution of a plane Alfvén wave numerically in a 2D Cartesian geometry, and compared it with the results obtained for a torsional wave in the cylindrical geometry. Snapshots of the

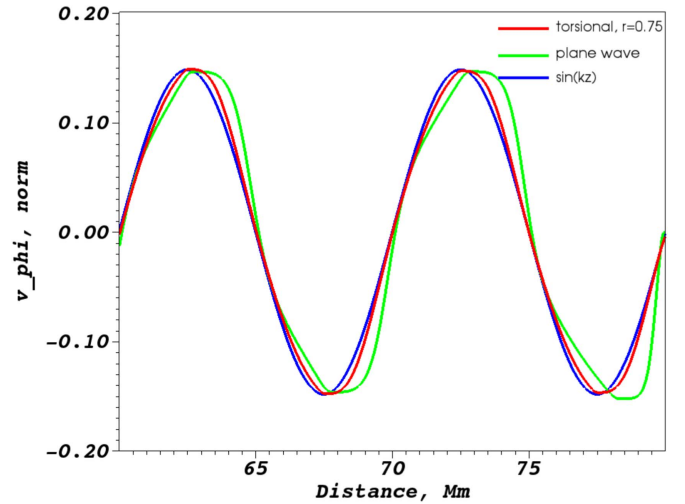


**Figure 5.** Comparison of snapshots of the azimuthal velocity  $v_\phi$  in a torsional wave (red) and perpendicular velocity in a plane Alfvén wave (green) of the same relative amplitude. The blue line shows a harmonic function that corresponds to the linear case. Both waves have propagated the distance of  $8\lambda = 80$  Mm from the point of the excitation. The amplitude of the torsional wave is measured at 0.75 Mm from the tube axis.

parallel, along the equilibrium field, structure of the steepened torsional and plane waves of the same amplitudes and wavelengths are shown in Figure 5.

The spatial profiles of both torsional and plane Alfvén waves clearly show the steepening: in the extremes, the perturbations in both the waves overtake the harmonic dependence. It occurs in both positive and negative extremes, which is a typical signature of the nonlinear evolution of linearly or elliptically polarized Alfvén waves (e.g., Cohen & Kulsrud 1974; Vasheghani Farahani et al. 2012). In the case of plane Alfvén waves, this effect is seen to be more pronounced, which is consistent with the results obtained by Vasheghani Farahani et al. (2012). However, in contrast to the long-wavelength limit, the decrease in the nonlinear steepening of the finite-wavelength torsional waves occurs even in the case of low- $\beta$ . It can be attributed to the presence of other sinks of energy, such as the excitation of the sausage mode.

### 3.6. Excitation of a Sausage Wave

The radial velocities  $v_r$ , that were nonlinearly generated by the torsional wave, have an axisymmetric structure, i.e., they are independent of the azimuthal coordinate. In a low- $\beta$  plasma, this spatial structure is similar to the structure of sausage (“ $m = 0$ ”) magnetoacoustic modes of the magnetic flux tube, which is an essentially compressive perturbation of the tube. Sausage modes are collective perturbations of the flux tube, and fill in the whole flux tube. Their specific properties, such as the radial structure and dispersion, are prescribed by the specific radial profile of the fast speed (e.g., Nakariakov et al. 2012; Yu et al. 2016). Consideration of this effect is out of scope of this paper.

In a low- $\beta$  plasma, a fast sausage mode propagates at the phase speed  $v_{\text{saus}}$ , which is lower than the Alfvén speed of external media  $C_A^{\text{ext}} = C_A(r \rightarrow \infty)$ , but higher than the Alfvén speed of plasma near the tube’s axis,  $C_A$  (Edwin & Roberts 1983). Because fast sausage modes are highly dispersive, a broadband pulse develops in a sausage wave train. For example, Shestov et al. (2015) numerically studied

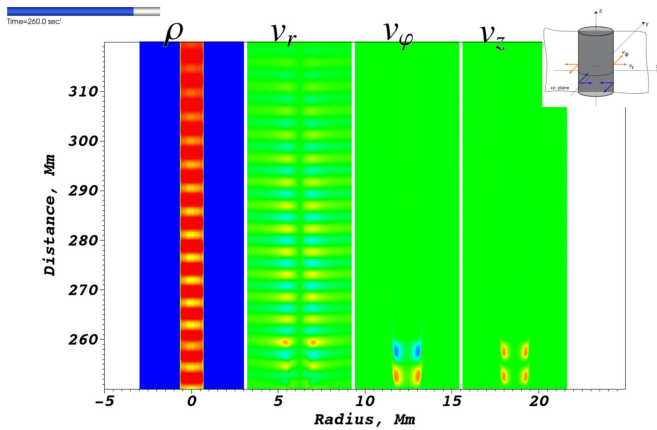


**Figure 6.** Spatial structure of perturbations in the vicinity of the leading front of the torsional wave, at the distance of  $26\lambda$  from the excitation point, at the time instant  $t = 260t_N = 188$  s.

the dispersive evolution of fast sausage wave trains guided by a magnetic flux tube, and confirmed the formation of wave trains with pronounced modulation of the instant period and amplitude. Also, it was found that the propagation speed is higher than the local Alfvén speed in the flux tube, and hence of the torsional wave. Thus, the nonlinearly induced fast sausage wave should propagate faster than the mother torsional wave.

Figure 6 shows the spatial structure of the incompressive and compressive perturbations in the vicinity of the leading front of the torsional wave, with the clear evidence of the fast sausage wave characterized by the perturbations of the density  $\rho$  and radial flows  $v_r$  preceding the torsional wave demonstrated by the perturbations of  $v_\varphi$  and the ponderomotively induced parallel flows  $v_z$ . The sausage perturbations are seen to propagate at the speed  $v_{\text{saus}} \approx 1.3C_A$ , which is consistent with the theoretical estimation of Edwin & Roberts (1983). The amplitude modulation of the sausage wave is also evident. Its amplitude varies in the  $z$ -direction, and, in particular, has a maximum at  $z \approx 280$  Mm at the instant of time of the snapshot shown in Figure 6.

### 3.7. Linear and Nonlinear Phase Mixing

The effect of linear phase mixing occurs near the tube boundary, where the local Alfvén speed gradually increases due to the decrease in the plasma density. The efficiency of phase mixing can be estimated using the following kinematic reasoning. The difference  $\delta$  between the distance traveled by the torsional perturbation near the boundary and in the body of the tube is equal to the product of the difference of the local Alfvén speeds at these radial surfaces,  $\Delta C_A$  and the travel time  $t$ . Thus the travel time required for phase mixing of one wavelength  $\delta = \lambda$  is the ratio of the wavelength in the body of the tube and the speed difference  $t = \lambda/\Delta C_A$ . The travel time is equal to the distance traveled by the wave from the source, divided by the Alfvén speed in the body of the tube  $t = z/C_A$ . Thus, the distance at which phase mixing reaches one wavelength is equal to  $z = \lambda C_A/\Delta C_A$ . In particular, in the numerical setup shown in Figure 1, the local Alfvén speed increases near the boundary by about  $\Delta C_A \approx 1.2 C_A$ , hence for the wavelength of 10 Mm the phase mixing reaches the wavelength at the distance of about 8.3 Mm from the wave

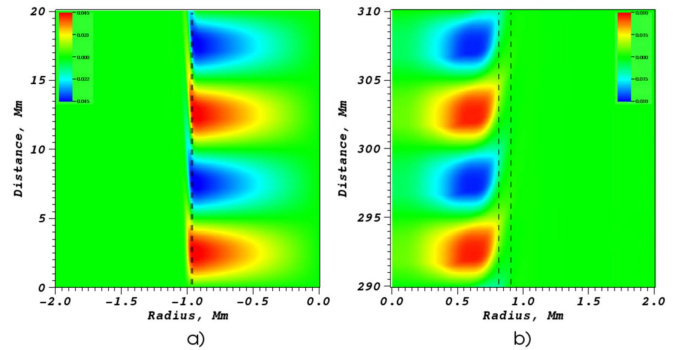


**Figure 7.** Comparison of linear and nonlinear phase mixing in a torsional Alfvén wave with the relative amplitude 0.05. Left: snapshot of the azimuthal velocity in the torsional wave that traveled 20 Mm from the source. Right: the same but at a distance of 310 Mm from the source. The vertical dashed lines highlight the radial distances discussed in the text.

source. This value is consistent with the deformation of the torsional wave front seen in the left panel of Figure 7.

Comparing the shapes of the torsional perturbations taken at different distances from the source in Figure 7, we see that at large distances from the source, the perturbation shape experiences some deformation even in the body of the flux tube. More specifically, near the source (left panel), the wave front is clearly deformed because of the non-uniformity of the local Alfvén speed in the region  $r > 0.95$  Mm. At  $r < 0.95$  Mm, near the source the wave fronts are symmetric with respect to the parallel coordinate. On the other hand, at a larger distance from the source (right panel), the wave front becomes clearly deformed even at the radial distances of  $r < 0.8$  Mm. This deformation has the typical signature of phase mixing: the perturbations at a larger radial distance from the axis propagate slightly faster. However, at these radial locations, the relative change of the local Alfvén speed is negligible. Thus, this phase mixing is not connected with the non-uniformity of the local Alfvén speed. The wave front deformation should be attributed to the variation of the propagation speed of the torsional wave caused by the variation of its amplitude with the radial coordinate. As the torsional wave amplitude increases in the radial direction, it causes additional radial non-uniformity of the torsional wave speed because of the nonlinear acceleration. It can further enhance phase mixing of torsional waves—the effect we shall refer to as “nonlinear phase mixing.” In the right panel, the torsional perturbation is absent from the region  $r > 0.8$  Mm, because of the numerical dissipation of the very strong phase mixing occurring in this region at much shorter distances from the source.

Following the reasoning used in the case of linear phase mixing, the distance at which nonlinear phase mixing reaches one wavelength is equal to the product of the wavelength and the ratio of the local Alfvén speed and the increase in the speed caused by the nonlinearity,  $z = \lambda C_A / \Delta C_A^{\text{nl}}$ , where  $\Delta C_A^{\text{nl}}$  is the difference in the local propagation speeds between the nonlinear and linear torsional waves. The increase in the local speed of the torsional wave,  $\Delta C_A^{\text{nl}}$ , is proportional to the product of the local Alfvén speed and the square of its relative amplitude (see the second term in the brackets on the right-hand side of Equation (22) of Vasheghani Farahani et al. 2012). As in the performed simulation, the relative amplitude of the torsional wave amplitude was 0.05, the effect of nonlinear phase mixing should be rather weak. More specifically, in this run, the efficiency of nonlinear phase mixing is more than a hundred times ( $0.05^2$ ) weaker than that of the linear phase



mixing that operates near the boundary. Indeed, according to Figure 7, at the distance of about 30 wavelengths from the source, phase mixing is equal to a fraction of the wavelength.

#### 4. Conclusions

We performed numerical simulations of axisymmetric finite-amplitude torsional Alfvén waves in a field-aligned magnetic flux tube filled in with a low- $\beta$  plasma. The flux tube is straight, untwisted, and non-rotating. The flux tube is surrounded by a plasma with the magnetic field directed in the same direction as inside the tube, in the direction of the tube axis. The plasma density inside the flux tube is enhanced, which makes the tube a fast magnetoacoustic waveguide. The plasma parameter  $\beta$  is taken to be small everywhere. The torsional perturbations are excited at one footpoint of the tube as alternate periodic azimuthal rotations of the tube. The wavelength of the driven torsional wave is of the same order as the diameter of the flux tube. In the linear regime, the torsional wave is incompressible and consists of the alternate azimuthal flows and the perturbations of the azimuthal component of the magnetic field.

We found that nonlinear evolution of the torsional Alfvén wave leads to the excitation of three different kinds of compressive motions that propagate along the axis of the magnetic flux tube: the well-known parallel flow of the plasma at the Alfvén speed; another parallel flow, at the tube speed, that is the slow magnetoacoustic wave; and, in addition, the mainly radial axisymmetric perturbations propagating at the speed higher than the Alfvén speed inside the flux tube, i.e., faster than the speed of the mother torsional waves. The latter kind of induced waves is the sausage fast magnetoacoustic modes. The sausage mode perturbs the plasma also outside the flux tube, which is consistent with the radial structure of sausage modes. Nonlinearly induced flows of all three kinds have double the frequency of the mother torsional wave.

The nonlinearly induced parallel plasma flow that propagates at the Alfvén speed can be considered as the “Alfvénic wind,” because its average over the oscillation period is not zero. The Alfvénic wind is absent from the vicinity of the flux tube axis, where the torsional wave amplitude is always zero. Thus, the parallel plasma flow that is nonlinearly induced by a torsional Alfvén wave has an annulus shape. The effect of Alfvénic wind has been concluded to be a possible mechanism for the acceleration of solar and stellar winds (e.g., Ofman & Davila 1998; Suzuki 2011), but those estimations were based on the assumption of plane Alfvén waves. Our study demonstrates that the field-aligned compressive flows induced by Alfvén waves in the solar and stellar coronae are essentially non-uniform in the transverse (e.g., the horizontal direction in the case of open magnetic configurations in coronal holes). There are always regions that are situated near the axes of the wave-guiding magnetic flux tubes, where the Alfvénic winds are zero. It may have important implications for the solar and stellar wind acceleration problems, which require a dedicated study.

The intrinsic radial non-uniformity of the torsional wave amplitude, which is connected with the need to satisfy the zero boundary condition at the axis of the flux tube, leads to the effect of nonlinear phase mixing. This effect is connected with the nonlinear increase in the wave speed at the radial shells where the wave amplitude is higher. It leads to the additional distortion of the torsional wave front and hence the generation

of progressively small scales in the radial direction. In particular, this effect should enhance the nonlinear generation of the sausage modes. For example, for a simple, linearly growing in the radial direction radial profile of the torsional wave amplitude, the wave front propagates faster near the flux tube boundary because of the nonlinear effects. Thus, phase mixing occurs even if the radial profile of the Alfvén wave is flat, when this effect is absent for linear Alfvén waves. Further investigation of this effect would be of interest.

The induced compressive flows modify the local Alfvén speed, causing the self-interaction of torsional Alfvén waves. It causes the wave profile steepening that is a signature of the nonlinear cascade along the field. The comparison of the nonlinear steepening of the torsional wave with this effect in a plane Alfvén wave of the same amplitude and wavelength showed that the efficiency of the parallel nonlinear cascade in a torsional wave is lower than in a plane Alfvén wave. It could be attributed to the presence of additional sinks for the torsional wave energy, for example, the excitation of the sausage wave. The steepening takes place at some radial distance from the flux tube axis, and is strongest where the torsional wave amplitude is highest, e.g., near the flux tube boundary in the case of a linear radial profile of the torsional wave amplitude.

For the linear profile of the torsional wave amplitude, we found that the amplitude of the induced parallel flows has a parabolic radial structure. It is not a surprise, as the amplitude of the parallel motions is proportional to the mother torsional wave amplitude squared: the parallel flows could not be nonlinearly induced near the flux tube axis, where the mother wave amplitude tends to zero. This result is different from the flat radial dependence assumed in the thin flux tube approximation given by expression (8). However, it does not show a problem with the thin flux tube approximation, because there the physical quantities are taken either at the flux tube axis or its boundary. The empirically determined best-fitting dependences of the radial profiles of the velocity vector components could be of interest for forward modeling of torsional waves, e.g., in the further development of the studies of Van Doorsselaere et al. (2016).

Our study demonstrates the importance of the transverse profile for the evolution of coronal torsional waves. The follow-up work should account for important effects of stratification, and the variation of the flux tube area and plasma temperature.

The work was partially supported by the Program for Fundamental Research of the Presidium RAS P7 “Experimental and theoretical investigations of solar system and star planetary system objects. Transitional and explosion process in astrophysics,” by Russian Science Foundation (RSF) grant No. 17-12-01567. S.V.S. acknowledges support from the Belgian Federal Science Policy Office through the ESA—PRODEX programme (grant No. 4000117262). V.M.N. acknowledges the support by the European Research Council under the *SeismoSun* Research Project No. 321141. The simulations were supported by the Supercomputing Center of Lomonosov Moscow State University (Sadovnichy et al. 2013) and at Royal Observatory of Belgium. The results of the simulations were analyzed with VisIt software (Childs et al. 2012). The authors are grateful to Chun Xia for his help with the MPI-AMRVAC code.



## Appendix A

### Weakly Nonlinear Torsional Waves in Thin Flux Tube Approximation

We illustrate the excitation of compressive perturbations by the analysis of long-wavelength weakly nonlinear torsional Alfvén waves. We consider perturbations of a straight cylindrical magnetic flux tube, using the cylindrical coordinate axis with the axis  $z$  coinciding with the flux tube's axis. A torsional Alfvén wave consists of alternate twisting azimuthal motions  $v_\varphi$  of the plasma, accompanied by the azimuthal components of the magnetic field  $B_\varphi$ . Since both quantities should vanish on the axis of the magnetic tube, torsional Alfvén waves could be considered in terms of the second order thin flux tube approximation of Zhugzhda (1996). In this approach, the parallel wavelength of the perturbations is taken to be much larger than the flux tube radius, which allows one to consider only a few lowest order terms in the Taylor expansion with respect to the radial coordinate,

$$\begin{aligned} \rho &\approx \tilde{\rho}, \quad p \approx \tilde{p} + p_2 r^2, \quad v_r \approx Vr, \quad v_\varphi \approx \Omega r, \quad v_z \approx u \\ B_r &\approx B_{r1} r, \quad B_\varphi \approx Jr, \quad B_z \approx \tilde{B}_z + B_{z2} r^2, \end{aligned} \quad (8)$$

where  $B_r$ ,  $B_\varphi$ , and  $B_z$  are the radial, azimuthal, and longitudinal components of the magnetic field, and  $v_r$ ,  $v_\varphi$ , and  $v_z$  are the radial, azimuthal, and parallel components of the velocity, respectively;  $V$ ,  $\Omega$ , and  $J$  are the radial derivatives of the radial and azimuthal components of the velocity, and the azimuthal field, respectively;  $\rho$  is the mass density; and  $p$  is the gas pressure. The quantities with the overtilde are the zeroth-order terms of the expansions with respect to the radial coordinate. The overtilde will be omitted hereafter. In the derivation of these equations it is assumed that the longitudinal wavelength of the perturbations is much larger than the radius of the flux tube.

Applying expansion (8) to the ideal MHD equations, and omitting terms with higher degrees of  $r$ , one obtains

$$\begin{aligned} \rho \left( \frac{\partial V}{\partial t} + u \frac{\partial V}{\partial z} + V^2 - \Omega^2 \right) + 2p_2 \\ + \frac{1}{2\pi} (J^2 + B_z B_{z2}) - \frac{1}{4\pi} B_z \frac{\partial B_{r1}}{\partial z} = 0, \end{aligned} \quad (9)$$

$$\frac{\partial \Omega}{\partial t} + u \frac{\partial \Omega}{\partial z} + 2V\Omega + \frac{J}{4\pi\rho} \frac{\partial B_z}{\partial z} - \frac{B_z}{4\pi\rho} \frac{\partial J}{\partial z} = 0, \quad (10)$$

$$\rho \left( \frac{\partial u}{\partial t} + u \frac{\partial u}{\partial z} \right) + \frac{dp}{dz} = 0, \quad (11)$$

$$\frac{\partial \rho}{\partial t} + \frac{\partial(\rho u)}{\partial z} + 2\rho V = 0, \quad (12)$$

$$\frac{\partial B_{r1}}{\partial t} + \frac{\partial(u B_{r1})}{\partial z} - \frac{\partial(V B_z)}{\partial z} = 0, \quad (13)$$

$$\frac{\partial J}{\partial t} + \frac{\partial(u J)}{\partial z} - \frac{\partial \Omega B_z}{\partial z} + 2VJ - 2\Omega B_{r1} = 0, \quad (14)$$

$$\frac{\partial B_z}{\partial t} + u \frac{\partial B_z}{\partial z} + 2B_z V = 0, \quad (15)$$

$$\left( \frac{\partial}{\partial t} + u \frac{\partial}{\partial z} \right) \frac{p}{\rho} = 0, \quad (16)$$

$$2B_{r1} + \frac{\partial B_z}{\partial z} = 0. \quad (17)$$

The effect of the gravitational force is neglected. All considered physical parameters are independent of the azimuthal coordinate, i.e.,  $\partial/\partial\varphi = 0$ . In other words, we restrict our attention to the consideration of the axisymmetric perturbations only.

The equations are supplemented by the magnetic flux conservation equation and total pressure balance at the tube boundary,

$$B_z A = \text{const}, \quad (18)$$

$$\begin{aligned} p + \frac{B_z^2}{8\pi} - \frac{A}{2\pi} \left[ \rho \left( \frac{\partial V}{\partial t} + u \frac{\partial V}{\partial z} + V^2 - \Omega^2 \right) \right. \\ \left. + \frac{1}{4\pi} \left( J^2 - \frac{1}{4} \left( \frac{\partial B_z}{\partial z} \right)^2 + \frac{B_z}{2} \frac{\partial^2 B_z}{\partial z^2} \right) \right] = p_T^{\text{ext}}, \end{aligned} \quad (19)$$

where  $A = \pi R^2$  is the cross-sectional area of the tube of radius  $R$ , and  $p_T^{\text{ext}}$  is the external total pressure.

The equations are linearized with respect to the equilibrium that is an untwisted and non-rotating flux tube,  $\rho_0$ ,  $p_0$ ,  $B_{z0}$ ,  $A_0$  (or  $R_0$ ), and  $u_0 = V_0 = J_0 = \Omega_0 = B_{r1}^0 = 0$ . All equilibrium quantities are constant.

In the linear regime, torsional motions are decoupled from compressible motions. Torsional perturbations given by  $\Omega$  and  $J$  and described by Equations (10) and (14),

$$\frac{\partial \Omega}{\partial t} - \frac{B_{z0}}{4\pi\rho_0} \frac{\partial J}{\partial z} = 0, \quad (20)$$

$$\frac{\partial J}{\partial t} - B_{z0} \frac{\partial \Omega}{\partial z} = 0, \quad (21)$$

which are readily combined in the wave equation

$$\frac{\partial^2 J}{\partial t^2} - C_A^2 \frac{\partial^2 J}{\partial z^2} = 0, \quad (22)$$

where  $\omega/k = C_A$  and  $C_A = B_{z0}/\sqrt{4\pi\rho_0}$  is the Alfvén speed. A harmonic torsional wave is  $J = J_M \cos(\omega t - kz)$  and  $\Omega = \Omega_M \cos(\omega t - kz)$ , where the constant amplitudes  $\Omega_M = -J_M/\sqrt{4\pi\rho_0}$ .

Compressive perturbations given by  $u$ ,  $V$ ,  $\rho$ ,  $p$ ,  $B_z$ , and  $A$ , and linked by Equations (11), (12), (15), (16), (18), and (19). Excluding all variables but  $u$ , one can readily obtain the wave equation

$$\frac{\partial^2 u}{\partial t^2} - C_T^2 \frac{\partial^2 u}{\partial z^2} = 0 \quad (23)$$

where  $C_T = C_A C_S / (C_A^2 + C_S^2)^{1/2}$  is the tube speed, and  $C_S = \sqrt{\gamma p_0 / \rho_0}$  is the sound speed. Equation (23) has a propagating wave solution  $u = U_m \cos(\omega t - kz)$ , where  $U_m$  is a constant amplitude, and  $\omega/k = C_T$ .

Consider the nonlinear interaction of torsional and compressible waves of finite amplitudes. Taking into account the quadratically nonlinear term containing the torsional variables in the derivation of Equation (23), we obtain the inhomogeneous wave equation

$$\frac{\partial^2 u}{\partial t^2} - C_T^2 \frac{\partial^2 u}{\partial z^2} = - \frac{R_0^2 C_T^2}{4\pi\rho_0 C_S^2} \frac{\partial}{\partial t} \left( J \frac{\partial J}{\partial z} \right). \quad (24)$$

The right-hand-side term of Equation (24) describes the ponderomotive force. The solution of the equation is a sum of solutions of the homogeneous and inhomogeneous equations, i.e., the longitudinal, or “tube” wave propagating at the tube speed,  $C_T$ , and the induced, “ponderomotive” wave propagating at  $C_A$ . The ponderomotive wave constitutes the Alfvénic wind.

If the torsional wave is driven by a harmonic oscillation with the frequency  $\omega$  at a certain location  $z = 0$ , the solution of the equation is

$$u = \begin{cases} u_T + u_p, & 0 < z < C_T t, \\ u_p, & C_T t < z < C_A t, \\ 0, & z > C_A t, \end{cases} \quad (25)$$

where the tube wave  $u_T(z, t)$  is

$$\begin{aligned} u_T &= \frac{R_0^2 J_M^2}{16\pi\rho_0 C_A} \{\cos[2\omega(t - z/C_T)] - 1\} \\ &= \frac{R_0^2 \Omega_M^2}{4C_A} \{\cos[2\omega(t - z/C_T)] - 1\}, \end{aligned} \quad (26)$$

and the ponderomotive wave  $u_p(z, t)$  is

$$\begin{aligned} u_p &= \frac{R_0^2 J_M^2}{16\pi\rho_0 C_A} \{1 - \cos[2\omega(t - z/C_A)]\} \\ &= \frac{R_0^2 \Omega_M^2}{4C_A} \{1 - \cos[2\omega(t - z/C_A)]\}. \end{aligned} \quad (27)$$

Equation (25) indicates that in the weakly nonlinear case, the torsional Alfvén wave induces parallel flows that consist of two motions, the tube wave  $u_T$  and the ponderomotive wave  $u_p$ , both of which have the amplitude  $R_0^2 \Omega_M^2 / 4C_A$  and the frequency that is double the driving frequency. These parallel flows are accompanied by the perturbations of the plasma density  $\rho$ . Hence the nonlinearly induced perturbations are compressive.

However, this formalism does not allow one to take into account the effect of nonlinear phase mixing, connected with the increasing non-uniformity of the torsional wave fronts across the equilibrium magnetic field.

### Appendix B Weakly Nonlinear Effects Associated with Alfvén Wave Phase Mixing

Consider a plane Alfvén wave in a plasma with a 1D non-uniformity of the Alfvén speed across the field. For simplicity, the plasma is taken to be of zero- $\beta$ . In this consideration, we follow the formalism developed in Botha et al. (2000). Let the equilibrium magnetic field of the strength  $B_0$  be directed along the  $z$ -axis. The equilibrium density of the plasma,  $\rho_0$ , varies in the  $x$ -direction. A linearly polarized Alfvén wave is characterized by the perturbations of  $B_y$  and  $V_y$ .

In the weakly nonlinear case, we can restrict our attention to the quadratically nonlinear terms only. In this case, the nonlinearly induced flows are described by the equations

$$\frac{\partial^2 V_z}{\partial t^2} = -\frac{1}{\rho_0} \left[ \frac{\partial}{\partial t} \left( B_y \frac{\partial B_y}{\partial z} \right) \right], \quad (28)$$

$$\frac{\partial^2 V_x}{\partial t^2} - C_A^2(x) \left( \frac{\partial^2 V_x}{\partial x^2} + \frac{\partial^2 V_x}{\partial z^2} \right) = -\frac{1}{\rho_0} \left[ \frac{\partial}{\partial t} \left( B_y \frac{\partial B_y}{\partial x} \right) \right]. \quad (29)$$

Both of these flows are essentially compressive because both cause the density perturbation

$$\rho = -\int \left[ \frac{\partial}{\partial x} (\rho_0 V_x) + \frac{\partial}{\partial z} (\rho_0 V_z) \right] dt. \quad (30)$$

Equation (28) is similar to Equation (24), in the zero- $\beta$  limit. It describes the nonlinear excitation of the parallel plasma flows by the Alfvén wave, the ponderomotive wave, or the Alfvénic wind. It is clear that the induced parallel flows have the highest speed at the magnetic field lines where the amplitude of the Alfvén wave is the highest.

Equation (29), which describes the nonlinearly induced perpendicular flows is essentially different. Its left-hand side describes freely propagating fast magnetoacoustic waves that are subject to refraction connected with the non-uniformity of  $C_A(x)$ . In particular, in a magnetic flux tube with the enhanced plasma density, this effect leads to the appearance of fast magnetoacoustic modes, for example, sausage modes (e.g., Nakariakov et al. 2012). The nonlinear excitation of the perpendicular compressive flows occurs when the Alfvén wave is non-uniform in the perpendicular direction. Because of Alfvén wave phase mixing, the right-hand-side term experiences continuous growth, magnifying the effect of the nonlinear excitation.

### References

- Alfvén, H. 1942, *Natur*, **150**, 405  
 Antolin, P., & Shibata, K. 2010, *ApJ*, **712**, 494  
 Bisnovatyi-Kogan, G. S. 2007, *MNRAS*, **376**, 457  
 Botha, G. J. J., Arber, T. D., Nakariakov, V. M., & Keenan, F. P. 2000, *A&A*, **363**, 1186  
 Charbonneau, P., & MacGregor, K. B. 1995, *ApJ*, **454**, 901  
 Chaston, C. C., Carlson, C. W., Ergun, R. E., & McFadden, J. P. 2000, *PhysS*, **2000**, 64  
 Cheng, C., Chen, L., & Chance, M. 1985, *AnPhy*, **161**, 21  
 Childs, H., Brugger, E., Whitlock, B., et al. 2012, in High Performance Visualization-Enabling Extreme-Scale Scientific Insight, ed. W. Bethel, H. Childs, & C. Hansen (Boca Raton, FL: CRC Press)  
 Cohen, R. H., & Kulsrud, R. M. 1974, *PhFl*, **17**, 2215  
 Cooper, F. C., Nakariakov, V. M., & Williams, D. R. 2003, *A&A*, **409**, 325  
 Copil, P., Voitenko, Y., & Goossens, M. 2008, *A&A*, **478**, 921  
 Cranmer, S. R. 2009, *LRSP*, **6**, 3  
 Edwin, P. M., & Roberts, B. 1983, *SoPh*, **88**, 179  
 Fedun, V., Verth, G., Jess, D. B., & Erdélyi, R. 2011, *ApJL*, **740**, L46  
 Fletcher, L., & Hudson, H. S. 2008, *ApJ*, **675**, 1645  
 Heyvaerts, J., & Priest, E. R. 1983, *A&A*, **117**, 220  
 Hollweg, J. V. 1971, *JGR*, **76**, 5155  
 Hood, A. W., Brooks, S. J., & Wright, A. N. 2002, *RSPSA*, **458**, 2307  
 Kudoh, T., & Shibata, K. 1999, *ApJ*, **514**, 493  
 Laming, J. M. 2015, *LRSP*, **12**, 2  
 Malara, F., Primavera, L., & Veltri, P. 1996, *ApJ*, **459**, 347  
 Matsumoto, T., & Suzuki, T. K. 2012, *ApJ*, **749**, 8  
 McLaughlin, J. A., De Moortel, I., & Hood, A. W. 2011, *A&A*, **527**, A149  
 Mikhalyaev, B. B., & Bembitov, D. B. 2014, *SoPh*, **289**, 4069  
 Murawski, K., Solov'ev, A., Musielak, Z. E., Srivastava, A. K., & Kraśkiewicz, J. 2015, *A&A*, **577**, A126  
 Nakariakov, V. M., Homsey, C., & Melnikov, V. F. 2012, *ApJ*, **761**, 134  
 Nakariakov, V. M., Ofman, L., & Arber, T. D. 2000, *A&A*, **353**, 741  
 Nakariakov, V. M., Roberts, B., & Murawski, K. 1997, *SoPh*, **175**, 93  
 Nakariakov, V. M., Roberts, B., & Murawski, K. 1998, *A&A*, **332**, 795  
 Ofman, L., & Davila, J. M. 1995, *JGR*, **100**, 23413  
 Ofman, L., & Davila, J. M. 1998, *JGR*, **103**, 23677  
 Poedts, S., & Boynton, G. C. 1996, *A&A*, **306**, 610  
 Porth, O., Xia, C., Hendrix, T., Moschou, S. P., & Keppens, R. 2014, *ApJS*, **214**, 4

- Ruderman, M. S. 1999, [ApJ](#), **521**, 851
- Ruderman, M. S., Berghmans, D., Goossens, M., & Poedts, S. 1997, [A&A](#), **320**, 305
- Sadovnichy, V., Tikhonravov, A., Voevodin, V., & Opanasenko, V. 2013, in *Contemporary High Performance Computing: From Petascale toward Exascale*, ed. J. S. Vetter (London/Boca Raton, FL: Chapman & Hall/CRC Press)
- Shestov, S., Nakariakov, V. M., & Kuzin, S. 2015, [ApJ](#), **814**, 135
- Srivastava, A. K., Shetye, J., Murawski, K., et al. 2017, [NatSR](#), **7**, 43147
- Suzuki, T. K. 2011, [SSRv](#), **158**, 339
- Tikhonchuk, V. T., Rankin, R., Frycz, P., & Samson, J. C. 1995, [PhPl](#), **2**, 501
- Tsiklauri, D., & Nakariakov, V. M. 2002, [A&A](#), **393**, 321
- Tsiklauri, D., Nakariakov, V. M., & Rowlands, G. 2003, [A&A](#), **400**, 1051
- Uberoi, C. 1995, [PhST](#), **60**, 20
- Van Doorselaere, T., Antolin, P., Yuan, D., Reznikova, V., & Magyar, N. 2016, [FrASS](#), **3**, 4
- Van Doorselaere, T., Nakariakov, V. M., & Verwichte, E. 2008, [ApJL](#), **676**, L73
- Vasheghani Farahani, S., Nakariakov, V. M., Van Doorselaere, T., & Verwichte, E. 2011, [A&A](#), **526**, A80
- Vasheghani Farahani, S., Nakariakov, V. M., Verwichte, E., & Van Doorselaere, T. 2012, [A&A](#), **544**, A127
- Williams, T., Taroyan, Y., & Fedun, V. 2016, [ApJ](#), **817**, 92
- Wójcik, D., Murawski, K., Musielak, Z. E., Konkol, P., & Mignone, A. 2017, [SoPh](#), **292**, 31
- Yu, H., Li, B., Chen, S.-X., Xiong, M., & Guo, M.-Z. 2016, [ApJ](#), **833**, 51
- Zheng, J., Chen, Y., & Yu, M. 2016, [PhyS](#), **91**, 015601
- Zhugzhda, Y. D. 1996, [PhPl](#), **3**, 10